

Cellulose-Nanofiber-Enabled 3D Printing of a Carbon-Nanotube Microfiber Network

Yuanyuan Li, Hongli Zhu, Yibo Wang, Upamanyu Ray, Shuze Zhu, Jiaqi Dai, Chaoji Chen, Kun Fu, Soo-Hwan Jang, Doug Henderson, Teng Li,* and Liangbing Hu*

Highly conductive and mechanically strong microfibers are attractive in energy storage, thermal management, and wearable electronics. Here, a highly conductive and strong carbon nanotube/nanofibrillated cellulose (CNT–NFC) composite microfiber is developed via a fast and scalable 3D-printing method. CNTs are successfully dispersed in an aqueous solution using 2,2,6,6-tetramethylpiperidinyl-1-oxyl (TEMPO) oxidized NFCs, resulting in a mixture solution with an obvious shear-thinning property. Both NFC and CNT fibers inside the all-fiber-based microfibers are well aligned, which helps to improve the interaction and percolation between these two building blocks, leading to a combination of high mechanical strength (247 ± 5 MPa) and electrical conductivity (216.7 ± 10 S cm $^{-1}$). Molecular modeling is applied to offer further insights into the role of CNT–NFC fiber alignment for the excellent mechanical strength. The combination of high electrical conductivity, mechanical strength, and the fast yet scalable 3D-printing technology positions the CNT–NFC composite microfiber as a promising candidate for wearable electronic devices.

Flexible, stretchable, and wearable electronics are attracting increasing scientific and industrial interest in recent studies.^[1] The applications are ranging from energy storage such as flexible batteries and supercapacitors to biomedical monitoring such as wearable contact lens.^[2] Conductive fiber, serving as an important component in wearable electronics, has gained tremendous attention by virtue of their high flexibility, knittability, and lightweight.^[3] 3D printing is a prototyping technology that enables transferring conductive ink into fibers and fiber-based 3D network structures. Successful demonstrations include 3D-printed batteries,^[4] embedded electronic sensors,^[5] embedded circuits,^[6] and supercapacitors.^[7]

Superb mechanical properties together with good electrical conductivity are necessary in order to meet the requirements

for flexibility and performance under severe deformation.^[8] Carbon nanotubes (CNTs) have been intensely studied as the building blocks to make mechanically strong and highly conductive microfibers due to their impressive mechanical properties and electrical conductivity.^[9] The elastic modulus and strength of CNTs are on the order of 1.0 TPa and 50 GPa, respectively, and their electrical conductivity reaches 10^6 S cm $^{-1}$ for single-wall CNTs and 3×10^4 S cm $^{-1}$ for multiwalled CNTs, respectively.^[10] However, such excellent properties cannot be fully employed when they are assembled into microscale structures due to the poor dispersion quality and alignment of the building blocks, and the unsatisfied load transfer between CNTs and a matrix.^[11] Dispersing CNT bundles into stable single CNTs in liquid is a challenge for the 3D spinning process due to the severe agglomeration

driven by the strong van der Waals forces among CNTs.^[12,13] Covalent modifications can help disperse CNTs. However, it usually destroys the electronic structure of CNTs, leading to lower conductivities and increased cost.^[14]

Nanofibrillated cellulose (NFC) with diameters in the nanoscale and lengths in the microscale is a promising polymer that can be used as a surfactant due to its amphiphilicity.^[15] Hamed et al. successfully demonstrated CNT dispersion using carboxy-methylated NFC through bath sonication.^[15c] Indeed, NFC possesses dimensions similar to CNTs, excellent mechanical properties, large surface area, and a low density.^[16] These properties make NFC an excellent building block to fabricate lightweight and strong materials suitable for structural applications,^[17] tissue engineering,^[18] and energy storage.^[19] Introducing nanocellulose in flexible and wearable electronics is getting increased attention. The successful demonstrations include touchscreen panel,^[20] transparent light-emitting diodes (LEDs),^[21] batteries,^[22] and stretchable origami electronics, etc.^[23] Based on the properties, NFC was applied as a surfactant to disperse CNTs into water as well as a building block to form strong, conductive microfibers through a 3D-printing process. Figure 1 demonstrates the transformation of NFC-dispersed CNT solution into microfiber network through 3D printing. When the NFC-dispersed CNT solution is extruded out from the head with shear rate, both CNT and NFC are aligned along the microfiber direction. The solvent exchange between water

Dr. Y. Y. Li, Dr. H. L. Zhu, Y. B. Wang, J. Q. Dai, Dr. C. C. J. Chen, Dr. K. Fu, S.-H. Jang, D. Henderson, Prof. L. B. Hu
Department of Materials Science and Engineering
University of Maryland
College Park, MD 20742, USA
E-mail: binghu@umd.edu
U. Ray, Dr. S. Z. Zhu, Prof. T. Li
Department of Mechanical Engineering
University of Maryland
College Park, MD 20742, USA
E-mail: lit@umd.edu

DOI: 10.1002/smtd.201700222

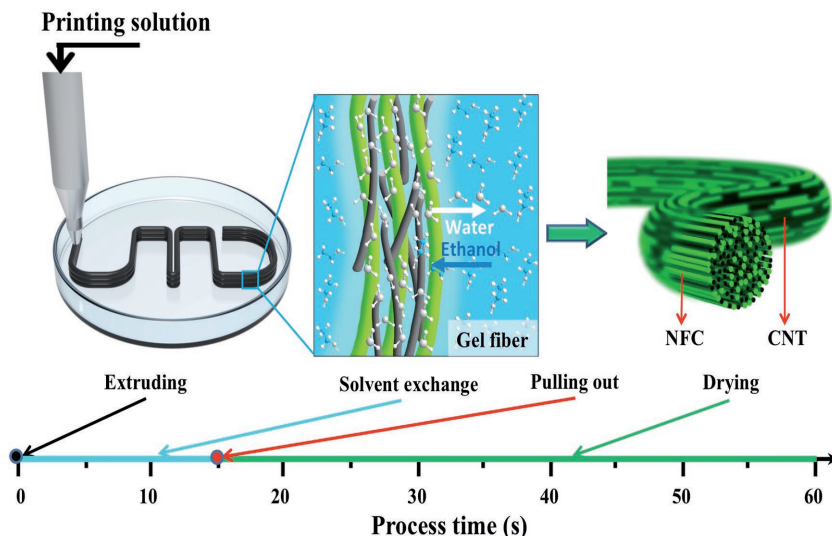


Figure 1. Schematic to show the CNT–NFC microfiber network formation through 3D printing. Solvent exchange was performed once the NFC-dispersed CNT solution was extruded into the coagulation bath of ethanol, leading to the formation of a stable gel fiber. A dry CNT–NFC microfiber can be obtained after pulling the gel fiber out to dry under tension for tens of seconds. During the process, all the building blocks are highly aligned along the fiber direction. The alignment of both CNT and NFC in microfibers leads to the combination of excellent mechanical strength and electrical conductivity.

and ethanol leads to gel fiber formation in the ethanol bath, which takes only a few seconds. The CNT–NFC microfibers with high alignment can be obtained by extracting the gel fibers from the ethanol followed by solvent evaporation.

Well-dispersed CNTs are the guarantee for a high-performance microfiber.^[12] In our design, NFC was used as a surfactant to disperse CNTs in water. It is pointed out that NFC-enabled CNT dispersion in water is the result of: i) the association

between CNT and NFC, and ii) stabilization with the help of NFC due to the steric hindrance and the electrostatic repulsive forces of NFC. There are different explanations about the association between NFCs and CNTs, including mechanical wrapping, the interaction between the hydrophobic sites of CNT and NFC, and the dipoles of sp^2 carbon lattice surface of the CNTs by the fluctuations of the counter ions on the surface of the NFC.^[24] We believe that the association is not the single effect of the above-mentioned mechanisms but a combination. In our case, hydrogen bonding between the hydroxyl and carboxyl groups on NFC and CNT also contributes, since the CNTs have been acid treated. Figure 2a lists the association between CNT and NFC through mechanical wrapping, hydrogen bonding between the hydroxyl and carboxyl groups on NFC and CNT, as well as the interaction between the hydrophobic sites of CNT and NFC. The CNTs are then stabilized due to steric hindrance of NFC and the electrostatic repulsive forces generated by the charged carboxyl groups. The NFCs were made through 2,2,6,6-tetramethylpiperidiny-

1-oxyl (TEMPO) oxidization followed by microfluidization with a diameter of about 20 nm and length in the microscale (Figure 2b). The zeta potential (ζ) value of the NFC solution was -64.9 mV, which leads to excellent stability of the solution. Without NFC, CNT can be partially dispersed in water by probe sonication due to the existence of carboxylic acid groups. However, large aggregates exist due to strong van der Waals forces between CNTs.^[25] With NFC, clear dispersion was obtained, as

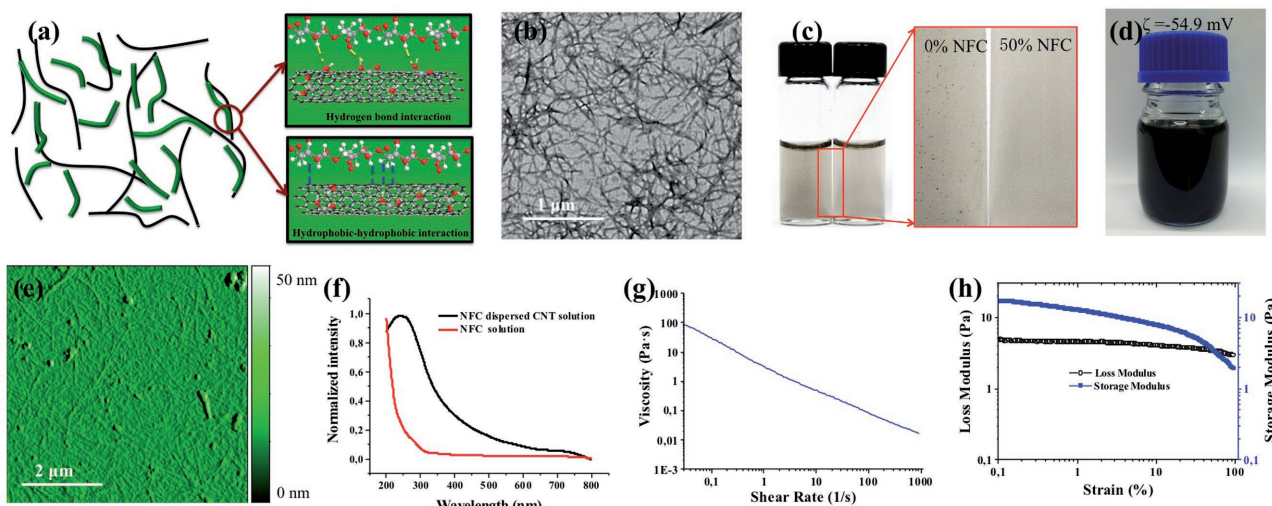


Figure 2. a) Schematic to show how NFC disperses CNT. Oxygen atoms are in red, hydrogen atoms are in white, and carbon atoms are in gray. b) TEM image of NFC. c) Optical images of CNT dispersed in water without (left) and with (right) NFC. d) A bottle of NFC-dispersed CNT solution with the ζ value of -54.9 mV. e) AFM image of NFC-dispersed CNT, showing individual fibrils arranged randomly and indicating the full dispersion of CNT. f) UV-vis spectroscopy of NFC and NFC-dispersed CNT water solution. g) The rheological properties of the CNT dispersion at the concentration of 0.5 wt% showing shear-thinning property. h) The viscoelastic properties of the CNT dispersion using strain sweep measurement.

shown in Figure 2c. This is due to the high electrostatic force of NFC, which prevents the aggregation. To characterize the stability of the dispersion, ζ potential of the NFC-dispersed CNT solution was tested. A ζ value of -54.9 mV was recorded, demonstrating good stability of the solution (Figure 2d). The CNT dispersion method is a potential large scalable method that more than 100 mL solution can be easily obtained in one batch in 30 min. Atomic force microscopy (AFM) was applied to characterize the NFC dispersed CNT solution. The root-mean-square roughness is 1.5 nm, which indicates good stability of the NFC-dispersed CNT solution. It is difficult to distinguish CNT from NFC from the AFM image (Figure 2e) because of their similar morphology. Thus, UV-vis spectroscopy was further employed to study the NFC-dispersed CNT solution.^[26] Figure 2f shows that the absorption peak appears at wavelength of about 250 nm, which indicates good dispersion of individual CNTs.^[15c] The viscosity of the NFC-dispersed CNT solution can be tuned by modifying the dispersion concentration through water evaporation. An obvious shear-thinning behavior was observed with the NFC-dispersed CNT solution (Figure 2g). The viscoelastic properties of the solution ready for printing were measured under strain sweep mode. Storage modulus was apparently larger than loss modulus when strain was less than 50% (Figure 2h). This indicates that the solution is in gel state, and a structural network exists in the system. As the shear strain increases, the storage modulus decreases, mainly due to the network breaking and fiber alignment introduced by shear stress. When shear strain was above 50%, storage modulus was lower than loss modulus, which means that the viscous deformation dominates, and the gel mainly responses liquid-like property. By modifying the viscosity through tuning concentration or introducing shear stress, the NFC-dispersed CNT solution was suitable to make either inks for a printing/writing

circuit or to be transferred into high-performance microfibers by 3D printing.

Using NFC as a dispersant for CNT dispersion is easy to scale up, and it holds more advantages than CNT dispersion through chemical modification. First, NFC can be extracted from abundant cheap resources, such as wood, cotton, and wheat straw. It is also bioactive because the NFC is biocompatible, and organic solvent is avoided. This makes the dispersion suitable for applications in life science and the disposal is a nonissue.^[27] Second, the dispersion of CNT is mainly based on absorption, wrapping, and fluctuation of counterions between the CNT and the NFC. Thus, the electronic structure and conductivity of individual CNT are preserved compared with dispersion by chemical modification.^[14,15c] In addition, the NFC remaining in the dispersion is an excellent building block to make strong, lightweight CNT nanocomposites.^[24b]

3D printing is a type of rapid prototyping that can achieve almost any complex geometric shape by control.^[28] This technique offers possibilities to realize printed 3D structural electronic devices such as capacitors, Li-ion batteries, and sensors.^[29] We demonstrated 1D fiber formation through 3D printing based on solvent exchange between ethanol and water. It is well known that CNT is not dispersible both in water and ethanol;^[30] thus, NFC was applied to disperse CNT in water while ethanol remained to be a poor solvent.^[15c] Figure 3a shows the conductive fiber fabrication process. The NFC-dispersed CNT aqueous solution was extruded into a coagulation bath of ethanol, where solvent exchange was performed to form a stable gel fiber. Then the gel fiber was pulled out and dried under tension at room temperature. The shear force introduced through extruding, and the tension applied during drying caused the building blocks to align along the fiber length direction, leading to a highly aligned microfiber.^[31]

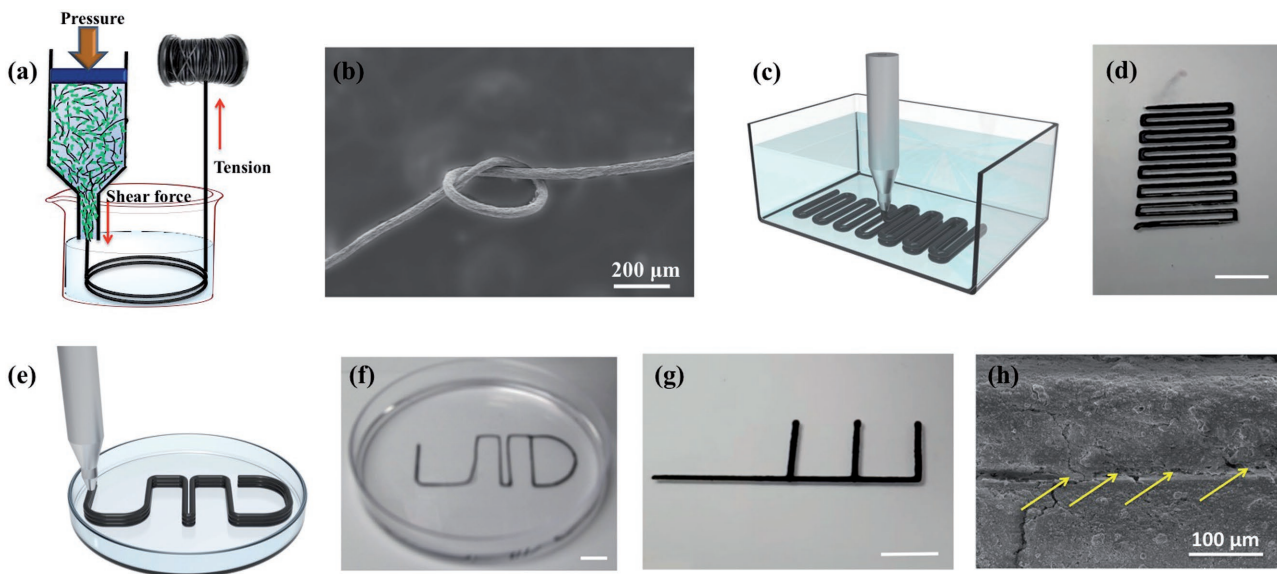


Figure 3. a) Schematic to show the fabrication of the microfiber, where the building blocks were prealigned by extruding into the coagulation and further aligned by tension during drying. b) A knot made from a microfiber showing the flexibility. c) Schematic image shows square-wave structure for 3D printing. d) 3D-printed square-wave structure. e) Designed “UMD” shape structure. f) Optical image of the “UMD” pattern precisely carried out through 3D printing. g) Programmable printed three-layered conductive lines with designed shapes. The scale bars in parts (d), (f), and (g) represent 10 mm. h) SEM image of the 3D-printed pattern showing the good adhesion between layers. The yellow arrows point the interface between two layers.

Good flexibility was demonstrated by making knots readily by hand, as shown in Figure 3b. The diameter of the microfibers decreases a lot during drying due to the solvent evaporation and shrinkage. The microfiber diameter is $19 \pm 4 \mu\text{m}$ when needles with an inner diameter of $150 \mu\text{m}$ were used. The fiber diameters can be varied through tuning the syringe needle diameters. More scanning electron microscopy (SEM) images of the microfibers obtained using needles with different diameters are shown in Figure S1 (Supporting Information). 3D square-wave structure can be printed with 1D microfibers as building blocks. The height of the structure is tunable by changing the overlapping number of printed fibers. Figure 3c and Figure 3d present a schematic image and a printed square-wave structural wall transferred from the schematic image, respectively. More complex structures can be achieved by gradually changing the position of the needle. A “UMD” pattern with combinations of circles and lines was first designed on the computer (Figure 3e). Figure 3f shows that the pattern was carried out precisely. The patterns were preserved after solvent evaporation. Video S1 in the Supporting Information demonstrates the 3D-printing process. Figure 3g shows the printed three-layered conductive line patterns with precisely controlled deposition position. To check the bonding between layers, SEM was carried out after carefully slow drying of the printed pattern where the printed structure is preserved. Figure 3h is the SEM image of the cross section from the printed pattern, indicating a good adhesion between layers. More patterns and SEM images are shown in Figure S2 (Supporting Information) to support the feasibility of 3D printing. The performance such as strength and conductivity for the final product is tunable through a programmable fiber assembly process. This technology has great potential in the fast fabrication of strong conductive electronics.

The performance of the 1D microfiber is the key for the final 3D-structured network for electronic devices; thereby, the microfibers obtained were carefully characterized. Small-angle X-ray scattering (SAXS) was applied to demonstrate the alignment. Due to the shear force during extruding and the tension during drying, CNTs and NFCs were aligned along the microfiber length direction. The shape of 2D SAXS pattern is a footprint of alignment at the nanoscale. A circular shape shows random orientation while an elliptical shape shows the alignment of building blocks.^[32] The 2D SAXS pattern of CNT–NFC fiber was in an elliptical shape (in the yellow contour), indicating the alignment in the fiber (Figure 4a). SEM was performed to provide direct observation of the building block alignment. Figure 4b is the low-magnification SEM image of the fiber showing fiber diameter of about $20 \mu\text{m}$. Figure 4c is the high-magnification SEM image showing the alignment of building blocks along the fiber direction. The alignment improves the percolation, and facilitates the stress and electron transfer between building blocks.^[33] In microscale, the alignment increases the fiber density, leading to lower defects and thus higher strength.^[34] Figure 4d is the typical stress–strain curve of the microfiber. The tensile strength of the microfibers can reach $247 \pm 5 \text{ MPa}$. The improvement in mechanical strength was mainly due to the alignment within the fiber and the presence of NFC, which is a strong building block and strengthening agent for the microfiber. The SEM image in the inset of Figure 4d shows that the building blocks are highly aligned along the fiber direction after mechanical testing. Papers were made by filtration of the same dispersion to prove the influence of alignment. In CNT–NFC filtered paper, SAXS patterns show a circular shape in the in-plane direction (Figure S3a, Supporting Information), which indicates the

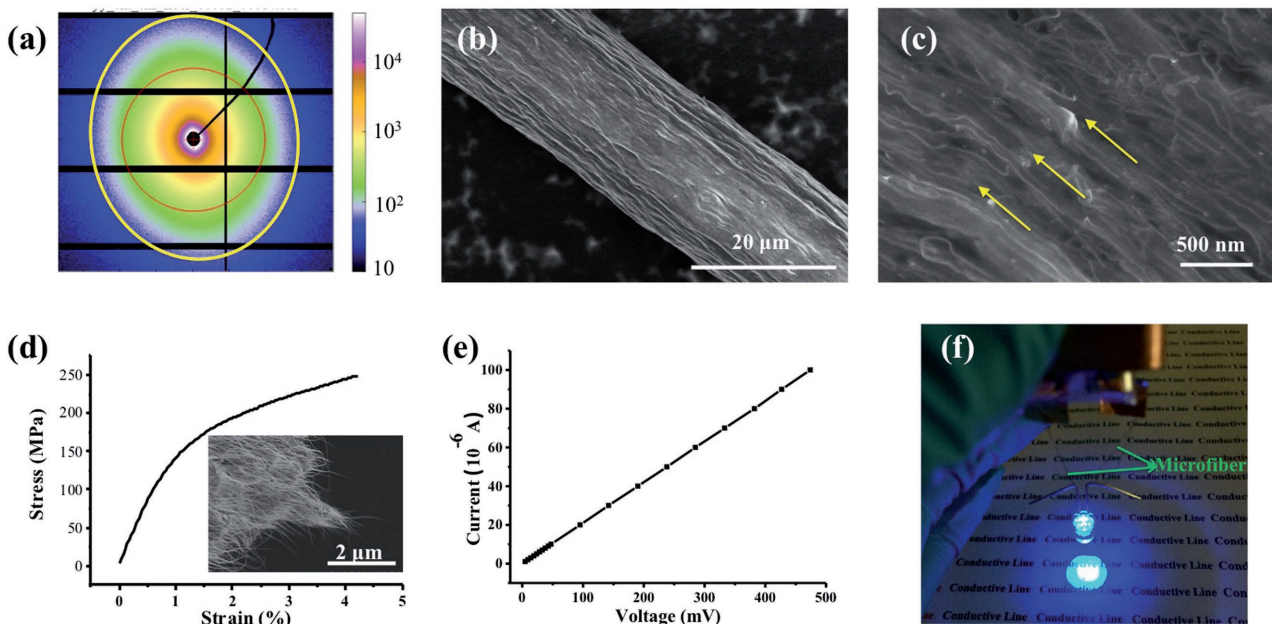


Figure 4. a) 2D SAXS pattern of the dry CNT–NFC microfiber. b,c) Low-magnification (b) and high-magnification (c) SEM images showing good alignment with building blocks aligned along the fiber direction. The yellow arrows indicate the alignment direction. d,e) Typical strain–stress curve (d) and I–V curve (e) of a microfiber with a diameter of $18 \mu\text{m}$; the inset in part (d) is the SEM image of a microfiber after tensile test. f) Microfiber as a conductive line to lift up and light an LED.

random orientation of building blocks. High-resolution SEM proved the random arrangement of building blocks in the planar direction of CNT–NFC paper (Figure S3b, Supporting Information). After mechanical testing, the average tensile strength of the paper is recorded as 156 MPa with a failure strain of 4.9%. The values are lower than that of the well-aligned microfiber, which is in good agreement with the above statement. Figure S3c (Supporting Information) shows the typical stress–strain curve of the CNT–NFC paper. A pure CNT film was also prepared, which has a tensile strength of 31 MPa.^[35] This value is much lower than that of the CNT–NFC film, indicating the reinforcing effect of NFC.

The dual alignment of both CNT and NFC in microfibers and the excellent dispersion quality of CNT by NFC also lead to excellent electrical conductivity. A high DC conductivity of $216.7 \pm 10 \text{ S cm}^{-1}$ was achieved in the mechanically strong microfibers. Figure 4e shows the typical *I*–*V* curve of the microfibers with a diameter of 18 μm . The obtained high-conductive microfibers can be applied in wearable electronic and energy storage devices.^[36] Figure 4f shows that an LED was lifted up and lighted by a battery with the mechanically strong and electrically conductive microfiber as a conductive line.

To provide fundamental insight into the role of aligned CNT–NFCs for mechanical property improvement in the microfiber, we carry out systematic atomistic modeling as detailed below. In our material system, the CNTs are decorated with carboxyl groups ($-\text{COOH}$) due to partial acid treatment. CNTs are well dispersed by NFC, and the CNT–NFC fiber shows strong alignment due to the shear force during extruding and the tension applied during drying. To understand the deformation and failure mechanics of the resulting microfiber, we construct an aligned CNT–NFC–CNT simulation model as shown in Figure 5a. Three single-walled CNTs in the top layer and three single-walled CNTs in the bottom layers are aligned (Figure 5a,b) with three cellulose molecular chains in the middle layer, respectively. To check the role of alignment, we also construct a control simulation model consisting of two layers of CNTs (three CNTs in each layer) in the top and bottom layers along with three cellulose molecular chains in the middle layer but in a direction perpendicular to the longitudinal axis of the CNTs, as illustrated in Figure 5c,d. This model is termed as the CNT–NFC–CNT not aligned model. Hydrogen bonds can form between the hydroxyl groups ($-\text{OH}$), carboxyl groups ($-\text{COOH}$) of the NFCs, and the carboxyl groups ($-\text{COOH}$) present in the CNT layers. Given that each repeating unit of cellulose molecule contains six hydroxyl groups, it is expected that in the CNT–NFC–CNT aligned model, significant amount of hydrogen bonds can form in between neighboring CNTs and NFCs, much more than those in the CNT–NFC–CNT not aligned model (Figure 5c,d). Given the ultrahigh strength of individual CNT and NFC, the tensile failure of the microfiber is expected to result from the relative sliding between neighboring CNTs and NFC. We simulate such a failure mechanism by sliding the two CNT layers relative to the NFC layer along the length direction in the CNT–NFC–CNT aligned model. For comparison, we also simulate the sliding of the top and bottom CNT layers relative to the middle NFC layer in the CNT–NFC–CNT not aligned model. Recent studies^[31,35,37] on tensile failure of cellulose nanopaper (made of a network of NFC nanofibers) and cellulose–graphene

oxide hybrid fiber reveal that, due to the facile formation nature of hydrogen bonds, the inter-fiber sliding involves a cascade of events of forming, breaking, and reforming of hydrogen bonds in between neighboring NFC nanofibers. Each hydrogen bond breaking dissipates energy. In sum, significant energy is needed to fracture the nanopaper by inter-fiber sliding (i.e., high toughness of the nanopaper).^[38] It is expected that the similar toughening mechanism holds in the CNT–NFC microfiber. Figure 5g plots the variation of total energy during the sliding process for the above two simulation models. Both curves feature a highly zigzag nature, which corresponds to a cascade of events of hydrogen bond forming (curve rising), breaking (curve dropping), and reforming (curve rising again), similar with that in the case of cellulose nanopaper and thus indicating the similar molecular-level toughening mechanism. The amplitude of the zigzags for the CNT–NFC–CNT aligned case is significantly larger (around three times) than that for the CNT–NFC–CNT not aligned case, showing clear evidence of the effect of the alignment on toughening the CNT–NFC microfiber. Figure 5h plots the variation of hydrogen bond energy during the sliding for the two simulation cases. From the difference in amplitude of zigzags in the hydrogen bond energy plots, it is evident that the NFC fibers in the aligned model undergo significantly larger amount of breaking and reforming of hydrogen bonds, and this substantially increases the resistance to sliding-induced mechanical failure of the microfiber, which finds its origin in the facile hydrogen bond formation due to rich hydroxyl groups in cellulose molecules. As a result, aligned CNT–NFC microfibers are effectively strengthened as well. In the CNT–NFC–CNT not aligned model, such breaking and reforming of hydrogen bonds are significantly lower. This can be readily understood as the significantly enhanced interfacial area in between neighboring CNTs and NFC chains if they are well aligned, which, in turn, leads to facile formation of hydrogen bonds between the neighboring CNTs and NFC chains. In other words, a microfiber with well-aligned CNTs and NFCs can dissipate much more energy and requires much higher stress during sliding-induced mechanical failure than a microfiber without CNT–NFC alignment, resulting in the high toughness and strength of the microfiber with good alignment. Also if Figure 5g and Figure 5h are observed closely, it can be seen that both the total energy and the hydrogen bond energy variation of each of the two models are very much similar. This indicates that for each model, majority of the energy, to withstand the tensile failure from sliding-induced loading, indeed stems from the hydrogen bonding. The more the density of hydrogen bonds, the greater the breaking and reforming of hydrogen bonds, and the better the mechanical performance of the material.

We used NFC to dramatically improve the 3D printability and mechanical/electrical properties of CNT microfibers based on the following mechanisms: i) NFC serves as an excellent dispersion agent to effectively disperse CNTs in solution; ii) 1D NFCs and CNTs lead to a high viscosity in dispersion, which is suitable for scalable fiber fabrication methods such as wet spinning and 3D printing; iii) the dual alignment of both CNTs and NFCs in microfibers leads to excellent mechanical strength/toughness and electrical conductivity at the same time. This work demonstrates that NFC is an excellent enabling material for high-performance microfibers for wearable electronics.

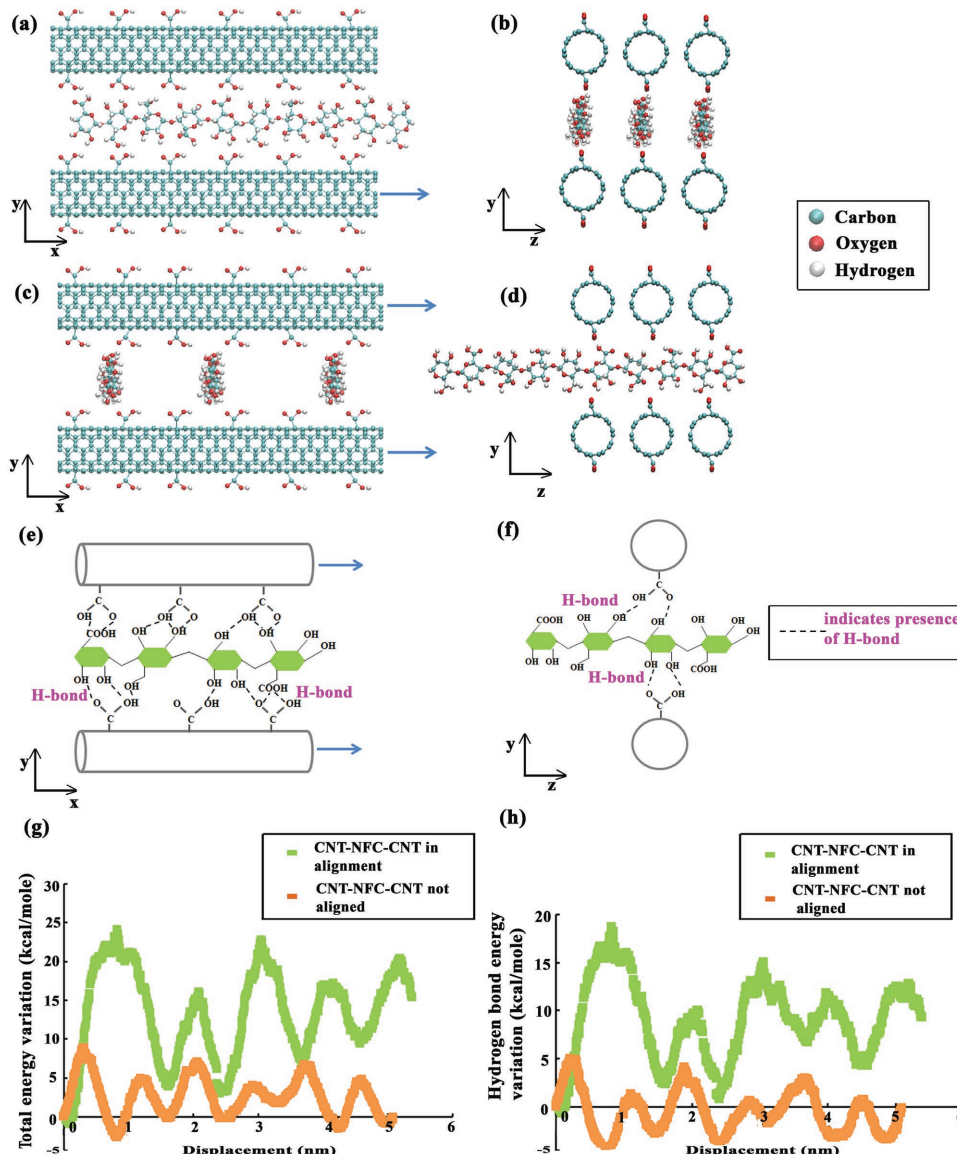


Figure 5. a,b) Side view and end view of molecular simulation model made of three layers: the top and bottom layers contain three CNTs each, and the middle layer contains three NFC chains. All CNTs and NFC chains are in parallel to each other. This model is termed as the aligned CNT–NFC–CNT model. c,d) Side view and end view of the CNT–NFC–CNT not-aligned model: three NFC chains in the middle layer are perpendicular to the CNTs in the top and bottom layers. e,f) Schematic illustrations showing more facile hydrogen bond formation in the CNT–NFC–CNT aligned model (e) than in the CNT–NFC–CNT not aligned model (f) due to interactions of rich hydroxyl groups in NFC interacting with the more number of $-COOH$ groups in CNTs for the aligned model. g,h) Variations of potential energy (g) and hydrogen bond energy (h) as a function of sliding displacement for the two models; the CNT–NFC–CNT aligned model (green) and the CNT–NFC–CNT not aligned model (orange) clearly demonstrate the effect of alignment on the superb toughness and strength of CNT–NFC microfibers. The zigzag nature of the curve in part (g) in addition to the significant difference in hydrogen bonding energy between the two models in part (h) reveal the molecular level toughening and strengthening mechanisms in aligned CNT–NFC microfibers.

Experimental Section

NFC Preparation: NFC was fabricated according to the literature.^[21] First, calculated TEMPO (78 mg), sodium bromide (514 mg), and never-dried Kraft bleached softwood pulp (5 g) were mixed together. Then, 30 mL of 12% NaClO were added into the mixture slowly to initiate TEMPO oxidation of the cellulose. During the oxidation process, the pH was maintained at 10.5 by adding 1 mol L⁻¹ NaOH. The reaction was run until NaClO was consumed. Agitation was applied throughout the process. After TEMPO treatment, the fibers were washed thoroughly

with distilled water and disintegrated into NFC by one pass through a Microfluidizer M-110EH (Microfluidics Ind., USA). The ζ potential was tested using the Zetasizer Nano ZS90 equipment to evaluate the stability of the dispersion. The concentration of NFC for the ζ potential test was 0.3 wt% with a pH value of 7.7 (Malvern Instruments, Malvern, UK). Transmission electron microscopy (TEM) JEOL JEM 2100 (Japan) was employed for the NFC morphology characterization with an accelerating voltage of 200 kV.

CNT Dispersion: CNT powder (P3, Carbon solution Inc.) and NFC were mixed together in water with a weight ratio of 1:1. The dispersion

process was performed by tube sonication for 20 min. The solution was centrifuged at the speed of 4000 rpm for 5 min, with the supernatant kept for characterization. The absorbance spectra of the CNT dispersions were obtained with a UV–Vis Spectrometer Lambda 35 (PerkinElmer, USA). The ζ potential was determined using the Zetasizer Nano ZS90 equipment with dispersion pH value of 7.8 (Malvern Instruments, Malvern, UK). AFM was applied to characterize the morphology of NFC-dispersed CNT.

CNT-NFC Microfiber Network Preparation and Characterization: The spinning solution was NFC-dispersed CNTs without centrifugation. The spinning solution was placed in a syringe connected to a stainless-steel needle with an inner diameter of 150 μm . Loaded syringes were then mounted in the 3D printer, where the position of the needle could be controlled by a computer program. 3D printing was operated with a bench-top robot (Fisnar F4200n) using a preprogrammed patterning procedure. The ink flow was controlled by an air-powered fluid dispenser (DSP501N, Fisnar). The nozzle pressure and printing speed were 50 psi and 10 mm s^{-1} , respectively. The 3D-printing process was performed through extruding the spinning solution directly into ethanol to form gel fibers according to the program. After the solvent exchange, printed stable pattern assembled from gel fibers were formed. The structure was preserved after solvent removal. To get microfibers, the gel fibers were pulled out from ethanol to dry in air. A force was applied at the ends of the fibers to allow the microfibers to dry under tension.

SEM JSM-7600F was used to characterize the morphology of the microfibers. The conductivity was calculated from the current–voltage (I – V) curve. Silver paste was painted at the end of the fiber and used as a contact point. Fiber length and average diameter for tensile testing were measured by optical microscopy. When calculating the conductivity, the fiber was treated as a perfect round shape. SAXS was performed to characterize the fiber alignment with an X-ray wavelength of $\lambda = 0.957 \text{ \AA}$ and a sample-to-detector distance of 8.422 mm. The beam size was 24 mm \times 11 mm (horiz. \times vert.), and a single-photon counting detector (Pilatus 1 M, Dectris) having the pixel size of 172 $\mu\text{m} \times 172 \mu\text{m}$ was used to record the scattering patterns.

Molecular Simulation Methodology: The molecular simulations were performed using the “Large-Scale Atomic/Molecular Massively Parallel Simulator” open-source package,^[39] and the potential used was the ReaxFF potential, which has been developed on the basis of the first principle and is appropriate for carbon–carbon interactions and hydrocarbon oxidation.^[40] This potential models the chemical bonding contributions to potential energy by bond order functions based on distances and can break down the total potential energy contribution into several subcategories including an explicit expression for hydrogen bonding. A (5,5) CNT with a length of 5 nm was used in our model. To model the acid-treated CNTs, –COOH functional groups were attached to each side of CNTs throughout, that was six number of –COOH groups on one face of a CNT and six more on the diametrically opposite face. One NFC chain in our model had five periodic units. The NFCs in the experiment were TEMPO treated. To model that, the –CH₂OH group was replaced at C6 position by a –COOH group such that one –CH₂OH group in every periodic unit was replaced by –COOH. Two models in total were used and each one of them comprised three layers—top, middle, and bottom. In the CNT–NFC–CNT aligned model, the top layer is with three CNT–COOH structures, the middle layer with three NFC chains parallel to the CNTs, and the bottom layer with three CNT–COOH structures. Bottom and top layers are the same. The CNT–NFC–CNT not aligned model is occupied by CNTs in the top and bottom layers as before but the NFCs in the middle layer are arranged perpendicular to the longitudinal axis of the CNTs. In the atomistic models, the vertical separation distance (in the y -direction) between each layer was kept constant for all cases, which is equal to 0.5 nm. The distance between CNTs center (in the z -direction) was also kept constant for all cases and equal to 0.1 nm. A time step of 0.5 fs was used throughout to make the simulations stable. Total energy and hydrogen bond energy data points were sampled after 200 time steps. The groups in all the layers were modeled as rigid bodies. Pulling was applied to the top and bottom layers at a constant translational velocity of 0.001 \AA fs^{-1} in the x -direction

while the entire structures in the middle layer was kept fixed. It was modeled as interactions between rigid structures and the explicit total potential energy and hydrogen bond energy values were obtained from the atomistic simulations.

Supporting Information

Supporting Information is available from the Wiley Online Library or from the author.

Acknowledgements

Y.Y.L., H.L.Z., Y.B.W., and U.R. contributed equally to this work. L.H. acknowledges the support from the DOD (Air Force of Scientific Research) Young Investigator Program (FA95501310143). L.H. and T.L. acknowledge the support from US National Science Foundation (Grant No.: 1362256). The authors would like to thank Dr. Shun Yu for the SAXS characterization of the microfiber at PETRA III, DESY. Yingxin Liu was acknowledged for the help of the rheology test.

Conflict of Interest

The authors declare no conflict of interest.

Keywords

3D printing, alignment, CNT dispersions, conductive and strong microfibers, molecular modeling

Received: June 17, 2017

Revised: July 4, 2017

Published online:

- [1] a) Y. Shang, X. He, C. Wang, L. Zhu, Q. Peng, E. Shi, S. Wu, Y. Yang, W. Xu, R. Wang, *Adv. Eng. Mater.* **2015**, *17*, 14; b) J. Lee, H. Kwon, J. Seo, S. Shin, J. H. Koo, C. Pang, S. Son, J. H. Kim, Y. H. Jang, D. E. Kim, *Adv. Mater.* **2015**, *27*, 2433.
- [2] a) J. Kim, M. Kim, M.-S. Lee, K. Kim, S. Ji, Y.-T. Kim, J. Park, K. Na, K.-H. Bae, H. K. Kim, F. Bien, C. Y. Lee, J. U. Park, *Nat. Commun.* **2017**, *8*, 14997; b) S. Ahmad, D. Copic, C. George, M. De Volder, *Adv. Mater.* **2016**, *28*, 6705.
- [3] a) Y. H. Lee, J. S. Kim, J. Noh, I. Lee, H. J. Kim, S. Choi, J. Seo, S. Jeon, T. S. Kim, J. Y. Lee, J. W. Choi, *Nano Lett.* **2013**, *13*, 5753; b) S. Lee, S. Shin, S. Lee, J. Seo, J. Lee, S. Son, H. J. Cho, H. Algadi, S. Al-Sayari, D. E. Kim, *Adv. Funct. Mater.* **2015**, *25*, 3114.
- [4] K. Sun, T. S. Wei, B. Y. Ahn, J. Y. Seo, S. J. Dillon, J. A. Lewis, *Adv. Mater.* **2013**, *25*, 4539.
- [5] H. Ota, S. Emaminejad, Y. Gao, A. Zhao, E. Wu, S. Challa, K. Chen, H. M. Fahad, A. K. Jha, D. Kiriy, *Adv. Mater. Technol.* **2016**, *1*, 1600013.
- [6] S. R. Shin, R. Farzad, A. Tamayol, V. Manoharan, P. Mostafalu, Y. S. Zhang, M. Akbari, S. M. Jung, D. Kim, M. Comotto, *Adv. Mater.* **2016**, *28*, 3280.
- [7] C. Zhu, T. Liu, F. Qian, T. Y.-J. Han, E. B. Duoss, J. D. Kuntz, C. M. Spadaccini, M. A. Worsley, Y. Li, *Nano Lett.* **2016**, *16*, 3448.
- [8] S. Pan, H. Lin, J. Deng, P. Chen, X. Chen, Z. Yang, H. Peng, *Adv. Energy Mater.* **2015**, *5*, 1401438.
- [9] a) B. Alemán, V. Reguero, B. Mas, J. J. Vilatela, *ACS Nano* **2015**, *9*, 7392; b) A. Lekawa-Raus, J. Patmore, L. Kurzepa, J. Bulmer, K. Koziol, *Adv. Funct. Mater.* **2014**, *24*, 3661.

- [10] a) W. Lu, M. Zu, J. Byun, B. Kim, T. Chou, *Adv. Mater.* **2012**, *24*, 1805; b) X. M. Sun, T. Chen, Z. B. Yang, H. S. Peng, *Acc. Chem. Res.* **2013**, *46*, 539.
- [11] a) K. Koziol, J. Vilatela, A. Moisala, M. Motta, P. Cunniff, M. Sennett, A. Windle, *Science* **2007**, *318*, 1892; b) W. H. Guo, C. Liu, X. M. Sun, Z. B. Yang, H. G. Kia, H. S. Peng, *J. Mater. Chem.* **2012**, *22*, 903.
- [12] C. Jiang, A. Saha, C. C. Young, D. P. Hashim, C. E. Ramirez, P. M. Ajayan, M. Pasquali, A. A. Martí, *ACS Nano* **2014**, *8*, 9107.
- [13] T. Chen, S. T. Wang, Z. B. Yang, Q. Y. Feng, X. M. Sun, L. Li, Z. S. Wang, H. S. Peng, *Angew. Chem., Int. Ed.* **2011**, *50*, 1815.
- [14] S. W. Kim, T. Kim, Y. S. Kim, H. S. Choi, H. J. Lim, S. J. Yang, C. R. Park, *Carbon* **2012**, *50*, 3.
- [15] a) I. Kalashnikova, H. Bizot, B. Cathala, I. Capron, *Langmuir* **2011**, *27*, 7471; b) Y. Li, H. Zhu, F. Shen, J. Wan, S. Lacey, Z. Fang, H. Dai, L. Hu, *Nano Energy* **2015**, *13*, 346; c) M. M. Hamedi, A. Hajian, A. B. Fall, K. Håkansson, M. Salajkova, F. Lundell, L. Wågberg, L. A. Berglund, *ACS Nano* **2014**, *8*, 2467.
- [16] a) A. Walther, J. V. I. Timonen, I. Diez, A. Laukkonen, O. Ikkala, *Adv. Mater.* **2011**, *23*, 2924; b) H. L. Zhu, Z. Q. Fang, C. Preston, Y. Y. Li, L. B. Hu, *Energy Environ. Sci.* **2014**, *7*, 269.
- [17] a) Y. Y. Li, H. L. Zhu, H. B. Gu, H. Q. Dai, Z. Q. Fang, N. J. Weadock, Z. H. Guo, L. B. Hu, *J. Mater. Chem. A* **2013**, *1*, 15278; b) Q. Z. Cheng, S. Q. Wang, T. G. Rials, *Composites, Part A* **2009**, *40*, 218.
- [18] K. Markstedt, A. Mantas, I. Tournier, H. c. Martínez Ávila, D. Hägg, P. Gatenholm, *Biomacromolecules* **2015**, *16*, 1489.
- [19] a) D. O. Carlsson, G. Nyström, Q. Zhou, L. A. Berglund, L. Nyholm, M. Stromme, *J. Mater. Chem.* **2012**, *22*, 19014; b) Y. Li, S. Yu, P. Chen, R. Rojas, A. Hajian, L. Berglund, *Nano Energy* **2017**, *34*, 541.
- [20] S. Ji, J. Jang, E. Cho, S. H. Kim, E. S. Kang, J. Kim, H. K. Kim, H. Kong, S. K. Kim, J. Y. Kim, J. U. Park, *Adv. Mater.* **2017**, *29*, 1700538.
- [21] H. L. Zhu, Z. G. Xiao, D. T. Liu, Y. Y. Li, N. J. Weadock, Z. Q. Fang, J. S. Huang, L. B. Hu, *Energy Environ. Sci.* **2013**, *6*, 2105.
- [22] G. Nyström, A. Marais, E. Karabulut, L. Wågberg, Y. Cui, M. M. Hamedi, *Nat. Commun.* **2015**, *6*, 7259.
- [23] S. Ji, B. G. Hyun, K. Kim, S. Y. Lee, S.-H. Kim, J.-Y. Kim, M. H. Song, J.-U. Park, *NPG Asia Mater.* **2016**, *8*, e299.
- [24] a) A. Hajian, S. B. Lindström, T. Pettersson, M. M. Hamedi, L. Wagberg, *Nano Lett.* **2017**, *17*, 1439; b) H. Koga, T. Saito, T. Kitaoka, M. Nogi, K. Suganuma, A. Isogai, *Biomacromolecules* **2013**, *14*, 1160; c) A. H. Mahiar, M. Hamed, A. B. Fall, K. Håkansson, M. Salajkova, F. Lundell, L. Wågberg, L. A. Berglund, *ACS Nano* **2014**, *8*, 2460; d) C. Olivier, C. Moreau, P. Bertoncini, H. Bizot, O. Chauvet, B. Cathala, *Langmuir* **2012**, *28*, 12463.
- [25] T. Premkumar, R. Mezzenga, K. E. Geckeler, *Small* **2012**, *8*, 1299.
- [26] L. Yue, G. Pircheraghi, S. A. Monemian, I. Manas-Zloczower, *Carbon* **2014**, *78*, 268.
- [27] H. Abdul Khalil, A. Bhat, A. Irene Yusra, *Carbohydr. Polym.* **2012**, *87*, 963.
- [28] C. B. Highley, C. B. Rodell, J. A. Burdick, *Adv. Mater.* **2015**, *27*, 5075.
- [29] a) J. T. Muth, D. M. Vogt, R. L. Truby, Y. Mengüç, D. B. Kolesky, R. J. Wood, J. A. Lewis, *Adv. Mater.* **2014**, *26*, 6307; b) B. G. Compton, J. A. Lewis, *Adv. Mater.* **2014**, *26*, 5930.
- [30] R. Rastogi, R. Kaushal, S. K. Tripathi, A. L. Sharma, I. Kaur, L. M. Bharadwaj, *J. Colloid Interface Sci.* **2008**, *328*, 421.
- [31] Y. Li, H. Zhu, S. Zhu, J. Wan, Z. Liu, O. Vaaland, S. Lacey, Z. Fang, H. Dai, T. Li, *NPG Asia Mater.* **2015**, *7*, e150.
- [32] K. M. O. Hakansson, A. B. Fall, F. Lundell, S. Yu, C. Krywka, S. V. Roth, G. Santoro, M. Kvick, L. P. Wittberg, L. Wagberg, L. D. Soderberg, *Nat. Commun.* **2014**, *5*, 4018.
- [33] X. Wang, N. Behabtu, C. C. Young, D. E. Tsentalovich, M. Pasquali, J. Kono, *Adv. Funct. Mater.* **2014**, *24*, 3241.
- [34] H. G. Chae, S. Kumar, *Science* **2008**, *319*, 908.
- [35] H. Zhu, S. Zhu, Z. Jia, S. Parvinian, Y. Li, O. Vaaland, L. Hu, T. Li, *Proc. Natl. Acad. Sci. USA* **2015**, *112*, 8971.
- [36] a) J. A. Lee, M. K. Shin, S. H. Kim, H. U. Cho, G. M. Spinks, G. G. Wallace, M. D. Lima, X. Lepro, M. E. Kozlov, R. H. Baughman, S. J. Kim, *Nat. Commun.* **2013**, *4*, 1970; b) J. Ren, L. Li, C. Chen, X. L. Chen, Z. B. Cai, L. B. Qiu, Y. G. Wang, X. R. Zhu, H. S. Peng, *Adv. Mater.* **2013**, *25*, 1155.
- [37] Z. Q. Fang, H. L. Zhu, Y. B. Yuan, D. Ha, S. Z. Zhu, C. Preston, Q. X. Chen, Y. Y. Li, X. G. Han, S. Lee, G. Chen, T. Li, J. Munday, J. S. Huang, L. B. Hu, *Nano Lett.* **2014**, *14*, 765.
- [38] H. Sehaqui, Q. Zhou, O. Ikkala, L. A. Berglund, *Biomacromolecules* **2011**, *12*, 3638.
- [39] S. Plimpton, *J. Comput. Phys.* **1995**, *117*, 1.
- [40] T. R. Mattsson, J. M. D. Lane, K. R. Cochrane, M. P. Desjarlais, A. P. Thompson, F. Pierce, G. S. Grest, *Phys. Rev. B* **2010**, *81*, 054103.